

Chapter 4

Classical-like wakes behind elliptical obstacles in Bose-Einstein condensates

4.1 Introduction

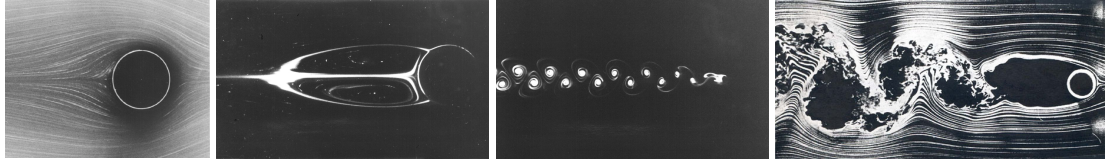


Figure 4.1: Classical viscous flow past a cylinder. From left to right: laminar flow ($Re = 3.64$) [67]; steady symmetric wake behind the cylinder ($Re = 41$) [67]; time-dependent Bénard–von Kármán vortex street ($Re = 112$) [68]; and chaotic downstream wake ($Re > 10^5$) [69].

Recent experimental [41, 42], numerical [70–72] and theoretical studies [73] have highlighted similarities between turbulence in quantum fluids and turbulence in ordinary (classical) fluids [74]. In particular, it is found that, in the idealized case of homogeneous isotropic conditions away from boundaries, the distribution of kinetic energy over the length scales obeys the celebrated Kolmogorov scaling of classical turbulence [75]. This similarity is remarkable, because a superfluid has zero viscosity and vorticity is not a continuous field. In the more realistic presence of boundaries such as an obstacle or confining channel walls, superfluid hydrodynamics is less understood, despite the large number of experiments in such scenarios.

In a classical viscous fluid [74], the prototype problem with a boundary is the flow around a cylinder or a sphere (or, changing the frame of reference, the motion of a cylinder or a sphere in a fluid at rest). The nature of such flow is determined by the Reynolds number

$Re = vd/\nu$, where v is the (assumed uniform) flow's velocity away from the obstacle, d is the obstacle's size, and ν is the fluid's kinematic viscosity. If $Re \lesssim 50$, a steady symmetric wake forms behind the obstacle; if $10^2 \lesssim Re \lesssim 10^5$ the wake becomes asymmetric and time dependent, forming the famous Bénard–von Kármán vortex street structure. For even higher values of Re , the flow becomes turbulent. These cases are depicted in Figure 4.1.

What happens in a superfluid is not clear. Firstly, the superfluid has zero viscosity ($\nu = 0$) and hence Re cannot be defined. Secondly, experiments performed in superfluid helium confirm that the flow is affected by the boundaries [76, 77]; unfortunately what is observed is not the flow pattern itself, but rather the trajectories of tracer particles, whose relation with the flow is still the subject of investigations [78]. Numerical simulations of three-dimensional (3D) superfluid flow around an oscillating sphere performed using the vortex filament model were not conclusive - quantum vortices did not appear to organise themselves into a visible classical-like wake near the obstacle [79–81].

Recent studies of the two-dimensional (2D) system have considered vortex emission and drag [82–86], the critical velocity [87–91], the effect of inhomogeneous potentials [85, 92, 93], the role of the obstacle parameters [86, 84, 94], and supersonic effects such as oblique dark solitons [95] and Cerenkov radiation [96]. In this chapter we discuss the rich variety of quantum wake regimes, often in close analogue to the classical counterparts, which can be obtained via the simple modification of the obstacle to an *elliptical* shape. We explore these dynamics in a homogeneous system, which serves to demonstrate the salient behaviour of superfluid flow past an elliptical obstacle, away from boundaries and density inhomogeneities which influence the vortex dynamics.

4.2 Model

We consider an atomic Bose-Einstein condensate (BEC) moving relative to a laser-induced obstacle (imposed through an external potential), as realized experimentally in 3D [97–99, 10] and quasi-2D condensates [10]. This scenario closely resembles that of the classical wake-problem [67, 68]. On a much larger scale, a similar 3D configuration has been experimentally realized in liquid helium [76, 77].

The BEC, parametrised by the wavefunction $\psi(\mathbf{r}, t)$ and assumed to be weakly-interacting and at ultracold temperature, is modelled through the GPE as described in Section 2.8.1, transformed into the moving frame as in Section 2.10.1. The external potential acting on the system $V(\mathbf{r}, t)$ is taken to be zero everywhere, apart from a localized repulsive potential which represents the obstacle with the Gaussian shape described in Section 2.15.2. A key feature of this work is that the obstacle is modified so that it has ellipticity ϵ , modifying the obstacle along the x axis, parallel to the flow. Such a potential can be generated via the repulsive optical dipole force from an incident blue-detuned laser beam which is

moved relative to the condensate either by deflection of the beam [97–99] or motion of the condensate itself when offset in a harmonic trap [10, 100, 101]. While laser-induced obstacles generated to date have had a circular profile, elliptical modification of the Gaussian potential can be achieved via cylindrical focussing of the laser beam.

The 2D (3D) system is simulated using the fourth-order Runge-Kutta method described in Section 3.1.1 under periodic boundary conditions on a 2048×512 ($400 \times 150 \times 150$) grid with uniform spacing $\Delta_x = 0.4\xi$. The computational box is sufficiently large that the boundary conditions do not play a role in vortex shedding. The initial condition is the stationary state of the GPE (including obstacle potential) with $v = 0$ as determined by the imaginary time convergence method described in Section 2.9. Setting $V_0 = 100\mu$ throughout, the external potential closely approximates an impenetrable obstacle. A small amount of noise is added to the initial condition to break symmetry: a random number between -0.0005 and 0.0005 is added to both the real and imaginary parts of the initial wavefunction. To minimize initial generation of waves, v is ramped up in time along a hyperbolic tangent curve, from $v = 0$ at $t = 0$ to its terminal value at $t \approx 200$ (ξ/c).

4.3 Two-Dimensional Wakes

4.3.1 Vortex emission from circular obstacles

The 2D scenario of an obstacle moving through a superfluid offers a simplified platform to consolidate analogues and disparities between classical and quantum fluids. In their pioneering simulations of the 2D nonlinear Schrödinger equation, Frisch *et al.* [102] observed the formation of vortex pairs in the flow past a circular obstacle. Although Frisch *et al.* considered a “hard” cylinder, it is also natural to employ a “soft” Gaussian potential (usually used in the context of atomic condensates). In practice this changes the quantitative, but not the qualitative, behaviour. Sasaki *et al.* [47] recently provided an extensive picture of 2D superflow past such a Gaussian obstacle. The flow regimes are depicted in Figure 4.2, based on simulations of the 2D GPE using similar parameters to [47]. At low flow velocity (a), the fluid undergoes smooth laminar flow around the obstacle. The streamlines of this flow are symmetric about $x = 0$, as in perfect potential flow. At a critical flow velocity, the local fluid velocity (which is highest at the poles of the obstacle) exceeds the speed of sound, breaking Landau’s criterion. Vortex pairs of opposite sign are nucleated periodically and drift downstream, forming a collimated wake of vortex pairs which are widely separated from each other (b). For higher velocities (c), alternating pairs of like-signed vortices are nucleated. At even higher velocities, vortex nucleation becomes highly irregular (d), forming a chaotic downstream distribution of vortices and sound (density) waves. These quantum fluid flow patterns bear some analogy to the classical flow patterns of Figure 4.1, particularly for the laminar flow and chaotic regimes. The alternating like-signed

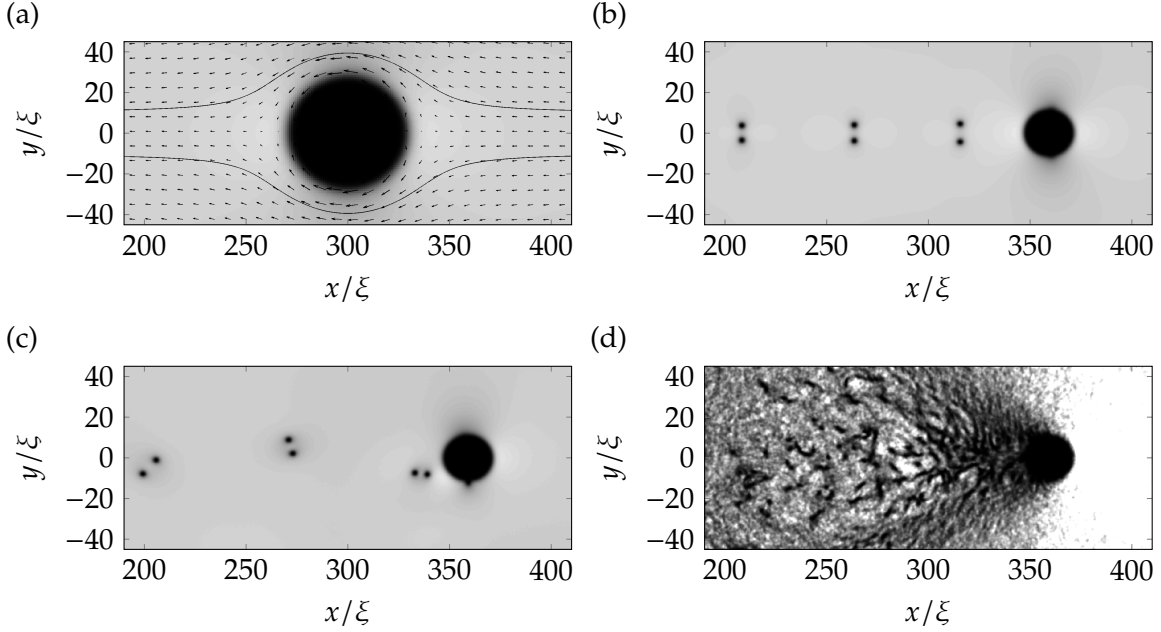


Figure 4.2: Condensate density during flow past a circular obstacle ($d = 5\xi$) at various flow speeds. For reference the critical velocity here is $v_c \approx 0.36 c$. (a) Laminar flow at a sub-critical flow speed ($v = 0.3 c$). The fluid velocity vector field and two streamlines illustrate the flow pattern. (b) Nucleation of vortex-antivortex pairs ($v = 0.365 c$). (c) Nucleation of like-signed vortex pairs ($v = 0.37 c$). (d) Chaotic vortex nucleation and generation of strong sound waves, forming a turbulent wake ($v = 0.9 c$).

vortices form a somewhat primitive analogue of the Bénard–von Kármán vortex street, while the vortex-antivortex pairs have no obvious classical analogue.

4.3.2 Vortex emission from elliptical obstacles

Consider, for illustration, an elliptical obstacle of size $d = 5\xi$ and ellipticity $\epsilon = 3$ moving at speed $v = 0.365 c$. This speed exceeds the critical velocity for the obstacle at that ellipticity, and so quantum vortices nucleate and trail behind the obstacle to form a wake [Figure 4.3(a)]. Sound waves generated by the obstacle have little effect on the vortex dynamics. At early times [Figure 4.3(a)(i)], the vortex shedding occurs through the symmetric generation of vortex-antivortex pairs, leading to a collimated and symmetric wake behind the obstacle. This is in qualitative agreement with observations for circular obstacles [102, 82, 85, 86] shown in Section 4.3.1, although for the same obstacle velocity and size, the elliptical obstacle induces a higher frequency of vortex emission and thus a denser wake.

At later times [Figure 4.3(a)(ii)], the flow becomes asymmetric due to the known instability of symmetric wakes [82]. A striking pattern emerges whereby distinct clusters of co-rotating vortices (of the order of 8 vortices in each cluster) develop downstream of the

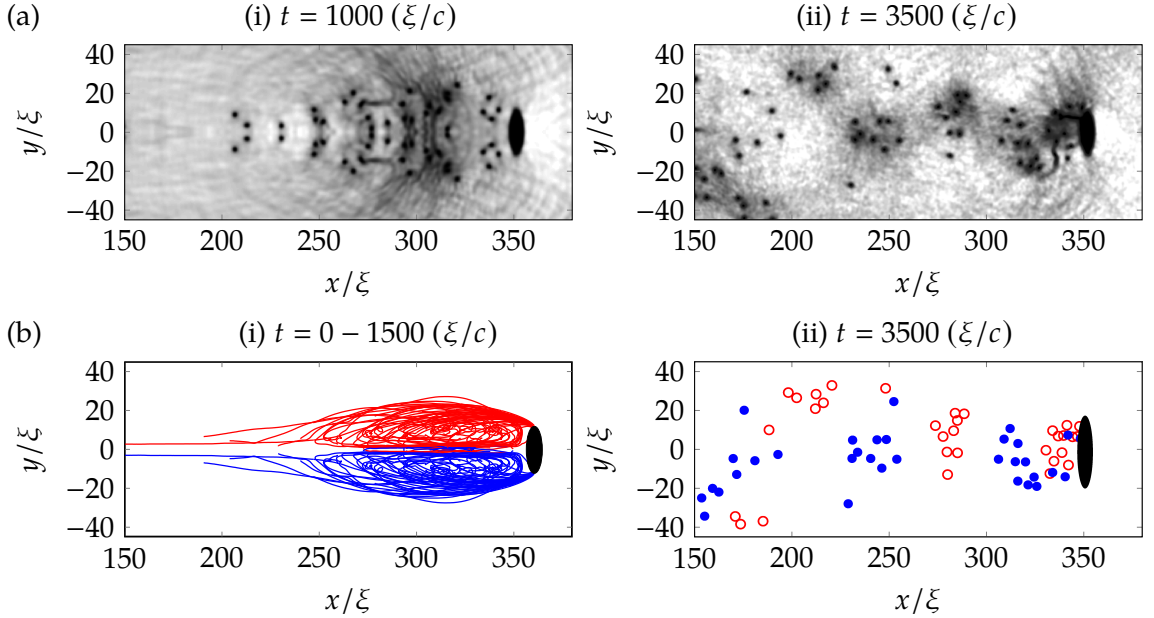


Figure 4.3: Snapshots showing the (a) density profile and (b) vortex trajectories during vortex shedding from an elliptical object ($\varepsilon = 3$) at (i) early times and (ii) later times. The obstacle has speed $v = 0.52c$ and size $d = 5\xi$. Red and blue lines represent vortices of oppositely quantized circulation. At early t , a symmetric wake similar to a classical fluid with low Re forms. Symmetry breaks at $t \approx 1500 (\xi/c)$ at which point vortex motion becomes disordered. In this case the initial condition is noise-free.

obstacle. Each cluster contains vortices of the same sign and adjacent clusters have alternating sign. These clusters form a Bénard–von Kármán vortex street downstream from the obstacle, confirming the intuition that a sufficiently large number of quanta of circulation reproduce classical physics. Here, the ellipticity of the obstacle facilitates the formation of this street; the relatively high rate of vortex emission leads to a greater interaction between vortices in the wake which in turn promotes clustering. This is in contrast to Section 4.3.1 where vortex pairs (clusters of only 2) are produced; the vortex emission rate and hence their subsequent interaction is insufficient to induce large scale clustering.

The vortex trajectories shown in Figure 4.3(b) provide visualisation of the time-integrated nature of the wake. At early times (i), we see that the vortex trajectories are symmetric, forming a flow pattern in striking analogue to the classical wake at low Re . The generic development of vortex trajectories is as follows. Pairs of singly-quantized vortices of opposite sign peel off from the poles of the obstacle and interact with each other as vortex-antivortex pairs. Each pair propagates in the positive x direction with approximate velocity $\hbar/(md_p)$ [47], where d_p is the pair separation [103]; the pair’s velocity is less than the obstacle’s velocity and so it drifts behind the obstacle. As the pair moves further away from the obstacle, its separation decreases and its velocity increases, such that it begins to catch the obstacle up. Once the pair is sufficiently close to the obstacle, it again separates and

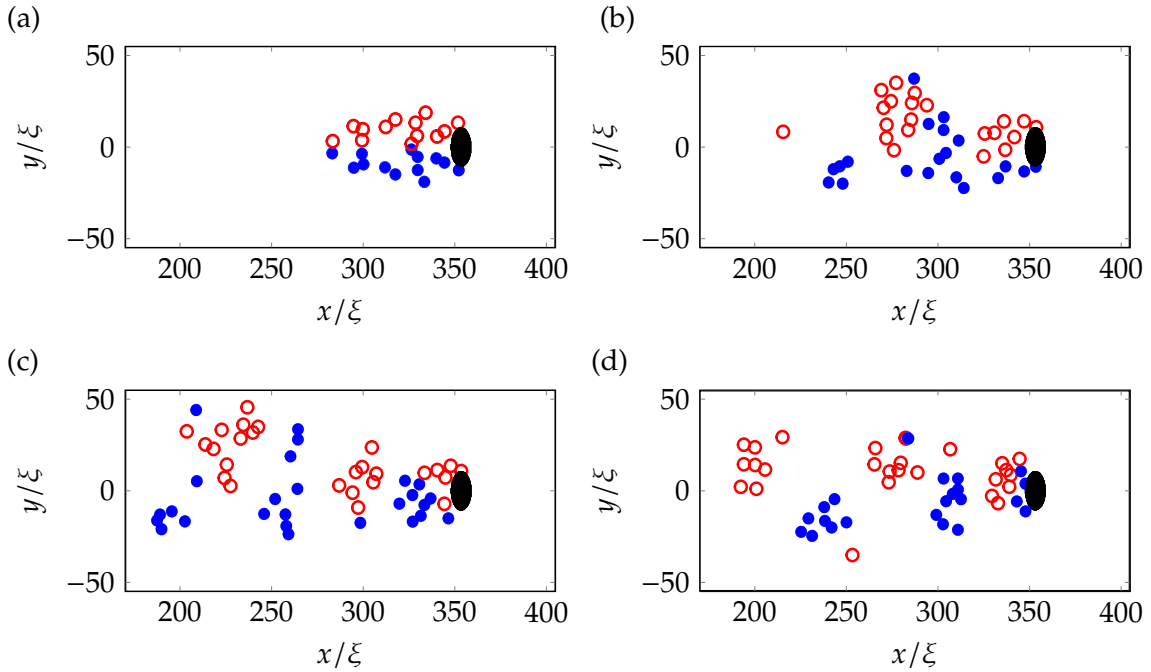


Figure 4.4: Snapshots of vortex locations during the motion of an elliptical object ($d = 5\xi$ and $\varepsilon = 3$) at speed $v = 0.52c$ in the presence of small-amplitude noise at $t = 0$. The snapshots are at times (a) $t = 450$, (b) 900 , (c) 1000 and (d) 1100 (ξ/c). Red/blue circles represent vortices with quanta of circulation $+1/-1$. The wake forms into clusters of like-circulation that continue to be produced, in analogy to the classical Bénard-von Kármán vortex street from a cylinder.

slows down, then the cycle repeats. As more vortices are nucleated, two distinct clusters of like-circulation form. Nucleated pairs then travel around the outside of the existing cluster before contracting, speeding up and travelling through the middle of the clusters towards the obstacle. The clusters grow until they reach a maximum size depending on the obstacle's size and speed. Hereafter, nucleated vortex pairs travel around the outside of the two clusters and continue travelling downstream, becoming lost from the main wake.

4.3.3 Formation of the Bénard–von Kármán vortex street

Once the symmetry of the wake is broken, vortices no longer separate into two distinct clusters of like-circulation. Existing vortices and newly-nucleated vortices mix together behind the obstacle. To accelerate the formation of the asymmetric wake, we subsequently seed the initial condition with noise. Figure 4.4 shows the vortex locations at various stages of the evolution. The initial symmetry of the wake [Figure 4.4(a)] breaks at $t \approx 450(\xi/c)$, with the wake splitting into several clusters. The velocity field around the obstacle is affected: it depends on time and the distance of the nearest cluster of vortices. The obstacle no longer simultaneously produces vortex-antivortex pairs, but now generates a series of like-signed vortices. Since like-signed vortices are known to co-rotate, these vortices group

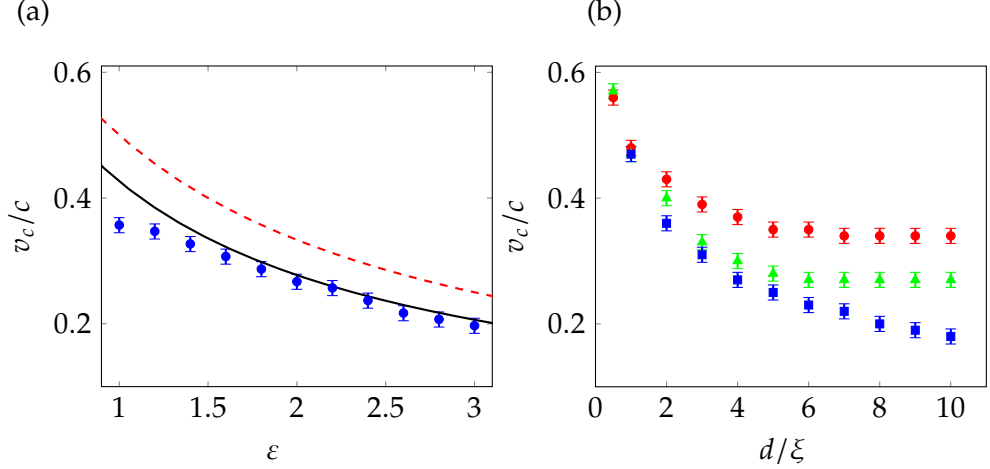


Figure 4.5: (a) Critical velocity against obstacle ellipticity ε , for $d = 10\xi$. Shown are the results the numerical simulations (blue bars), Equation (4.1) (dashed red line) and Equation (4.3) (solid black line). (b) Critical velocity (obtained numerically) versus the obstacle width d , for ellipticity $\varepsilon = 1$ (red circles), $\varepsilon = 2$ (green triangles) and $\varepsilon = 3$ (blue squares).

into clusters which slowly rotate. This cluster effects the velocity field once more, causing a cluster of opposite signed vortices to be produced. This process then repeats such that clusters of like signed vortices are then produced behind the obstacle, much like vorticity in the classical vortex street behind a cylinder. While some positive clusters contain negative vortices and vice versa, the overall pattern is still a time-dependent Bénard–von Kármán vortex street.

For clusters consisting of pairs of vortices, it has been shown that they can survive downstream for a very long time [47]. However, for regimes with larger numbers of vortices in each cluster, the chaotic nature of vortex motion can cause originally tightly packed and circular clusters to easily stretch over large areas, form strange shapes, or even split into smaller clusters. Examples of this can be seen later in Figure 4.6.

4.3.4 Critical Velocity past an Elliptical Obstacle

We now investigate in what ways the ellipticity of the obstacle affects the critical velocity for vortex nucleation and nucleation frequency. Figure 4.5(a) shows the critical velocity for flow past the obstacle as a function of its ellipticity, taking the obstacle to have fixed width in the y -direction of $d = 10\xi$. We determine the critical velocity numerically by performing simulations with flow velocities increasing in steps of $\Delta_v = 0.01 c$ until vortices nucleate. For a circular object, we find that the critical velocity is $v_c = 0.355 \pm 0.005 c$, consistent with predictions in the Eulerian ($d \gg \xi$) limit [89–91]. As the ellipticity is increased (i.e. the obstacle becomes narrower in x), the critical velocity decreases. The modification of the critical velocity is significant: if $\varepsilon = 3$, v_c is more than 40% smaller than that for a circular

obstacle.

The rough dependence of v_c on ε can be derived as follows. According to Landau's criterion [104], superfluidity breaks down when the fluid velocity exceeds the critical velocity $v_{\text{Lan}} = \min [E(p)/p]$, where p is the momentum of elementary excitations and $E(p)$ their energy. The weakly-interacting Bose gas has the dispersion relation $E(p) = [ngp^2/m + p^4/(4m^2)]^{1/2}$, hence $v_{\text{Lan}} = c$.

If an obstacle moves through the fluid with speed v , the local fluid velocity is enhanced near the obstacle so that the maximum local velocity, v_{max} , exceeds v . By approximating the BEC as an inviscid Euler fluid, the local velocity around the obstacle can be calculated using the complex variable framework of potential flow. The maximum local velocity is found to be at the poles with $v_{\text{max}} = (1 + \varepsilon)v$ [105], and the estimated Landau critical velocity becomes,

$$\frac{v_{c1}}{c} = \frac{1}{1 + \varepsilon}. \quad (4.1)$$

This estimate is shown as dashed red line in Figure 4.5(a), capturing the general shape of the relationship, but not the exact values for v_c .

Equation (4.1) is derived for incompressible potential flow, however, the GPE describes a compressible fluid and so the local density, $n(\mathbf{r}) = |\psi|^2$, in regions of high velocity is reduced. Ignoring the quantum pressure, the density (and therefore speed of sound) is reduced according to Bernoulli's equation [106],

$$1 + \frac{v^2}{2} = n(u) + \frac{u^2}{2}, \quad (4.2)$$

where $u(\mathbf{r})$ is the local velocity. We substitute the maximum local velocity, $v_{\text{max}} = (1 + \varepsilon)v$, into Equation (4.2) to find the local density at that point,

$$n(v_{\text{max}}) = 1 + \frac{1}{2}[1 - (1 + \varepsilon)^2]v^2.$$

The local speed of sound is $c_{\text{local}} = \sqrt{n}$ and so at the point of maximal velocity,

$$c_{\text{local}} = \sqrt{1 + \frac{1}{2}[1 - (1 + \varepsilon)^2]v^2}.$$

We use the resulting local speed of sound and the Landau criterion to find a corrected estimate of the critical velocity for the break down of superfluidity,

$$\frac{v_{c2}}{c} = \left[\frac{3}{2}(1 + \varepsilon)^2 - \frac{1}{2} \right]^{-\frac{1}{2}}. \quad (4.3)$$

This relation [solid black line in Figure 4.5(a)] gives good agreement with the computed values of v_c . The deviation for $\varepsilon \sim 1$ has been noted elsewhere [90], and can be remedied

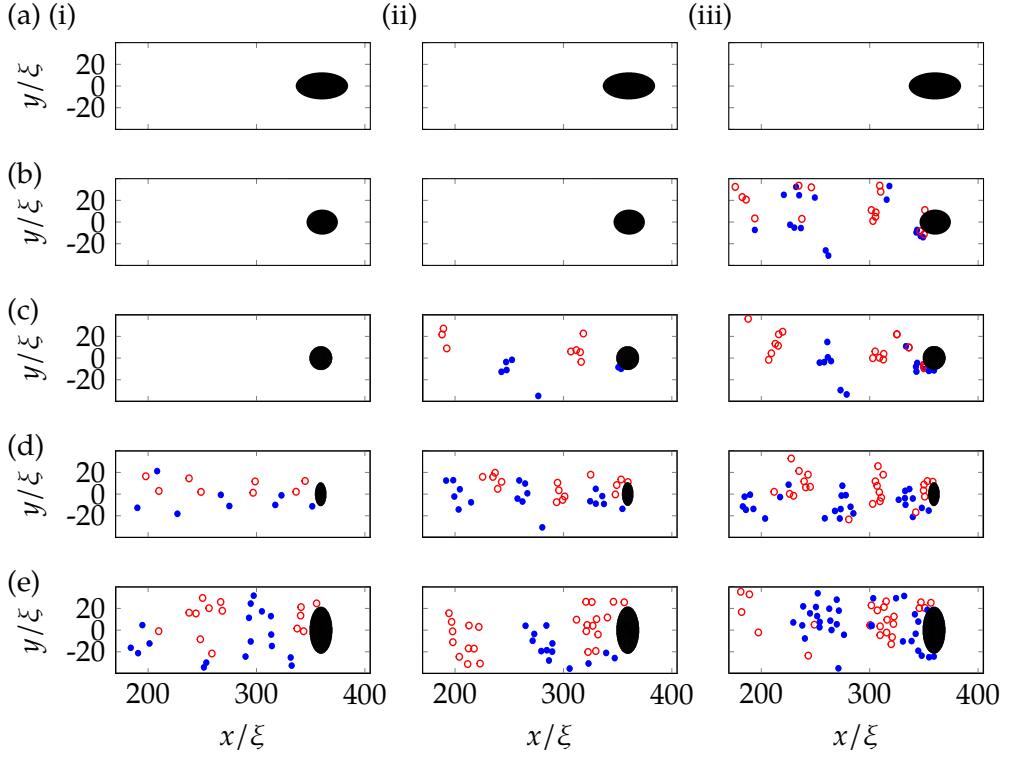


Figure 4.6: Snapshots of the vortex positions for various obstacle parameters, at $t = 2000$ (ξ/c). Shown are obstacles corresponding to (a) $\varepsilon = 0.5$ and $d = 5\xi$, (a) $\varepsilon = 0.75$ and $d = 5\xi$, (c) $\varepsilon = 1$ and $d = 5\xi$, (d) $\varepsilon = 2$ and $d = 5\xi$, and (e) $\varepsilon = 2$ and $d = 10\xi$, at the velocities (i) $v = 0.32c$, (ii) $v = 0.40c$, and (iii) $v = 0.48c$. Red/blue circles represent vortices with quanta of circulation $+1/-1$.

using higher order corrections taking into account the quantum pressure term.

From studies on circular objects, it is known that v_c depends on the obstacle's shape at small diameters, where boundary layer effects are significant; v_c approaches the "Eulerian" value only for large diameters $d \gg \xi$ [86, 90]. The variation of v_c with the obstacle width d is shown in Figure 4.5 (b). For $d = 10\xi$, the critical velocity effectively reaches its asymptotic value, while at smaller widths, it is much larger.

4.3.5 Role of Obstacle Size and Ellipticity on the Wake

During the initial symmetric phase of vortex nucleation, the wakes generated by the obstacle have the same qualitative structure shown in Figure 4.3(b) (i). However, once the wake becomes asymmetric, the nature of the clusters that form are highly dependent on the velocity and shape of the obstacle. Figure 4.6 shows wakes generated for various obstacle parameters, all captured at the same time $t = 2000$ (ξ/c). As predicted in the previous section, for an increased ε , the critical velocity for vortex nucleation is reduced. Conversely, reducing $\varepsilon < 1$ causes the critical velocity to increase to the point of no vortices being produced for any of the tested velocities. By visual inspection of the clusters that form in

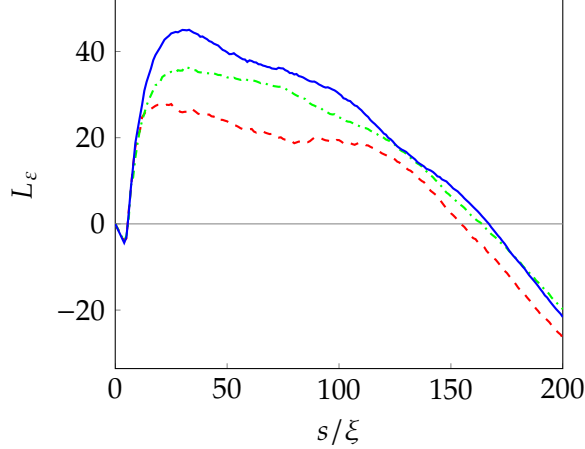


Figure 4.7: The clustering measurement $L_\varepsilon(s)$ for the three ellipticities $\varepsilon = 1$ (red dashed line), $\varepsilon = 2$ (green dot-dashed line), and $\varepsilon = 3$ (blue solid line) (with obstacle size $d = 5\xi$) averaged over 5 simulations for each ε with external flow velocities $v = 0.4, 0.425, 0.450, 0.475, 0.5 c$.

Figure 4.6, it can be seen that that any increase of size, ellipticity or velocity of the obstacle increases the number of vortices in the wake's clusters. We further explore this clustering behaviour and explain its roots in Section 4.3.6.

4.3.6 Vortex Clustering

We have shown that the Bénard–von Kármán vortex street forms through the clustering of like-signed vortices. Methods of quantifying the clustering of vortices in quantum fluids have been explored in the literature [48, 49, 62] and are described in detail in Section 3.3.

We begin by quantifying the effect of ellipticity on vortex clustering using Ripley's K and Besag's L functions defined in Section 3.3.2. To interpret the results, the curve

$$L_\varepsilon(s) = \langle \hat{L}(\varepsilon, s) - s \rangle, \quad (4.4)$$

is calculated. Here s characterises the radius of the clustering and $\hat{L}(\varepsilon, s)$ is the estimate of Besag's L curve given by Equation (3.8), measured at the time $t = 2500 (\xi/c)$ for the three ellipticities $\varepsilon = 1, 2, 3$. The average is performed for each value of ε , over 5 simulations with external flow velocities $v = 0.4, 0.425, 0.450, 0.475, 0.5 c$. When $L_\varepsilon(s) > 0$, it is interpreted as evidence of clustering on the scale of s for ellipticity ε . Conversely when $L_\varepsilon(s) < 0$, it is interpreted as evidence of a sparsity of vortices (as compared to randomly placed points in space) on the scale of s for ellipticity ε . The resulting curves are shown in Figure 4.7.

All three curves show pronounced evidence of clustering at scales of $5\xi \lesssim s \lesssim 150\xi$. Lack of clustering is evident at $s \lesssim 5\xi$, this is to be expected: multiply charged vortices are unstable, preferring to decay into several vortices distinct in space, and so clustering

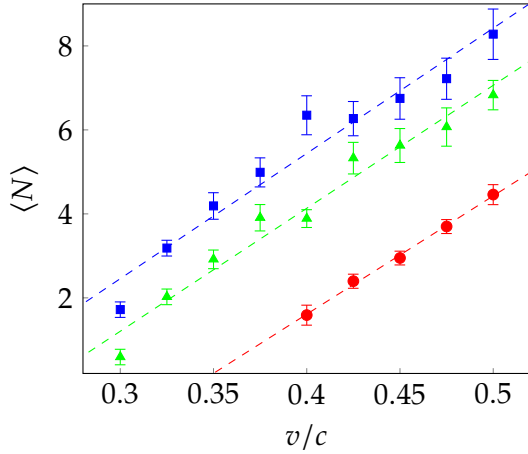


Figure 4.8: Average number of vortices in the clusters as a function of the obstacle velocity v . Shown are cases with $\varepsilon = 1$ (red squares), $\varepsilon = 2$ (green circles) and $\varepsilon = 3$ (blue triangles) with $d = 5\xi$. Also shown is are linear fits to the data for each value of ε .

is not expected on scales smaller than the radius of a vortex core (approximately 5ξ). The lack of clustering at scales of $s \gtrsim 150\xi$ can be explained by the lack of vortices far from the obstacle in the $\pm y$ directions. As ε increases, the peak value of $L_\varepsilon(s)$ also increases, showing evidence that an increase of ellipticity causes an increase of the spacial clustering of vortices in the fluid.

The $L_\varepsilon(s)$ measurement of clustering is entirely based on the K and L functions. These functions quantify the average spatial statistics of vortex clustering, but do not tell us the number of vortices present in clusters. We now utilize the more sophisticated Recursive Cluster Algorithm (RCA) of Reeves *et. al.* [49] (described in Section 3.3.3) to identify the number of vortices contained in clusters for different ellipticities and velocities. The use of RCA allows us to investigate how both velocity and ellipticity each affect vortex clustering. We record the number of clusters N_c and the number of vortices in each cluster N_i , where i is the cluster index. Then we determine the average number of vortices in the clusters, $\langle N \rangle = (1/N_c) \sum_{i=1}^{N_c} N_i$ as a function of obstacle velocity v for three ellipticities $\varepsilon = 1, 2$ and 3 , at times $t = 500, 510, \dots, 2500$ (ξ/c). The results, plotted in Figure 4.8, show that increasing v (above the critical velocity) causes $\langle N \rangle$ to increase and that, at fixed v , $\langle N \rangle$ increases with ε .

The behaviour of the quantities explored in this section, and therefore the reason that elliptical obstacles are efficient at producing classical-like wakes, can be explained by considering the shedding frequency of vortices. It is known that the shedding frequency increases with the velocity of the flow [83] and for an elliptical obstacle, the combination of a reduced critical velocity and increased local velocity around the obstacle has the effect of increasing the shedding frequency with ε and d . The overall result is that, when increasing any of v , ε or d , vortex shedding frequency is increased and so more vortices are nucleated

in a given time period, causing the cluster size to increase (explaining the behaviour of L_ε , $\langle N \rangle$, and the vortex clustering variation in Figure 4.6). By further simulation at large obstacle velocity ($v \gtrsim 0.6$), we also find that for all values of ε , the large velocity causes vortices to nucleate non-periodically, inducing an irregular flow without a visible Bénard–von Kármán vortex street configuration, in agreement with previous simulations with circular obstacles of smaller diameter [47].

4.4 Three-Dimensional Wakes

We now generalize our results to 3D by considering quantum wakes in three-dimensional flow past a localized obstacle, as simulated via the 3D GPE with the 3D obstacle potential of Equation (2.44). Our results will confirm that the features observed in 2D wakes also arise in the 3D setting. A comprehensive study of the parameter space is, however, not tractable in 3D due to the computational intensity of large scale 3D simulations.

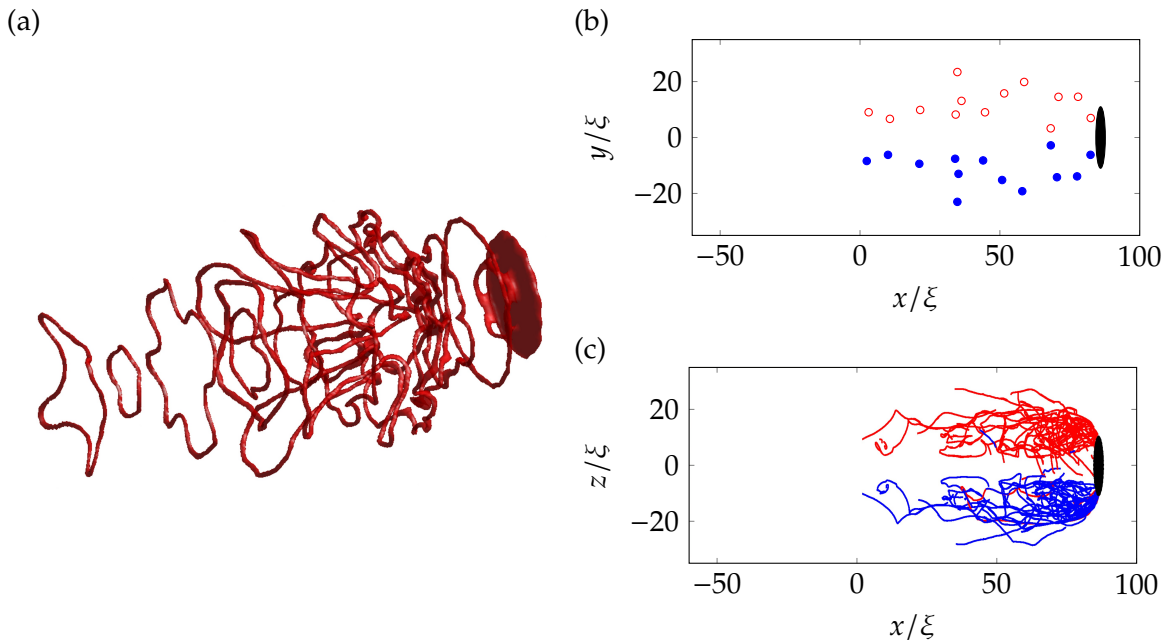


Figure 4.9: Symmetric wake in 3D at $t = 450$ (ξ/c) for an elliptical obstacle ($d = 5\xi$ and $\epsilon = 5$) moving at $v = 0.6 c$. (a) Isosurface plot of low density, over a range $[0, 100]$ in x and $[-25, 25]$ in y and z . (b) Vortex locations in the xy plane. (c) Vortex trajectories in the xz plane. In (b) and (c) red/blue denotes vortex lines with quanta of circulation $+1/-1$.

4.4.1 Symmetric Wakes

For a spherical ($\varepsilon = 1$) object with $d = 5\xi$, we find that the critical velocity is $v_c = 0.455 \pm 0.05 c$, consistent with $v_c = 0.55 c$ reported in the Eulerian limit ($d \gg \xi$) [106, 107]. Making

the obstacle ellipsoidal, with the short direction parallel to the flow, reduces the critical velocity, in parallel with our 2D observations. For example, for $\varepsilon = 5$, the critical velocity is reduced to $v_c = 0.315 \pm 0.05 c$. Figure 4.9(a) shows the 3D wake generated past this ellipsoidal obstacle ($d = 5\xi$ and $\varepsilon = 5$) when moving at super-critical speed $v = 0.6 c$. Vortex rings, the 3D analogue of vortex-antivortex pairs, are ejected at high frequency (due to the obstacles high ellipticity) in the direction of the flow. At early times ($t = 450 (\xi/c)$ in this case) the vortex configuration maintains cylindrical symmetry about the obstacle's axis, as is clearly visible in the xy and xz planes in Figure 4.9(b) and (c). As the vortex rings move downstream they shrink and speed up, returning to the object, sometimes passing through other vortex rings. A similar behaviour is observed [108] in the evolution of toroidal bundles of many coaxial vortex rings which leapfrog around each other. Occasionally a ring will escape this cycle and fall downstream. These behaviours lead to the formation of an organized symmetric wake behind the obstacle, the 3D analogue of our 2D observations.

4.4.2 Asymmetric Wakes

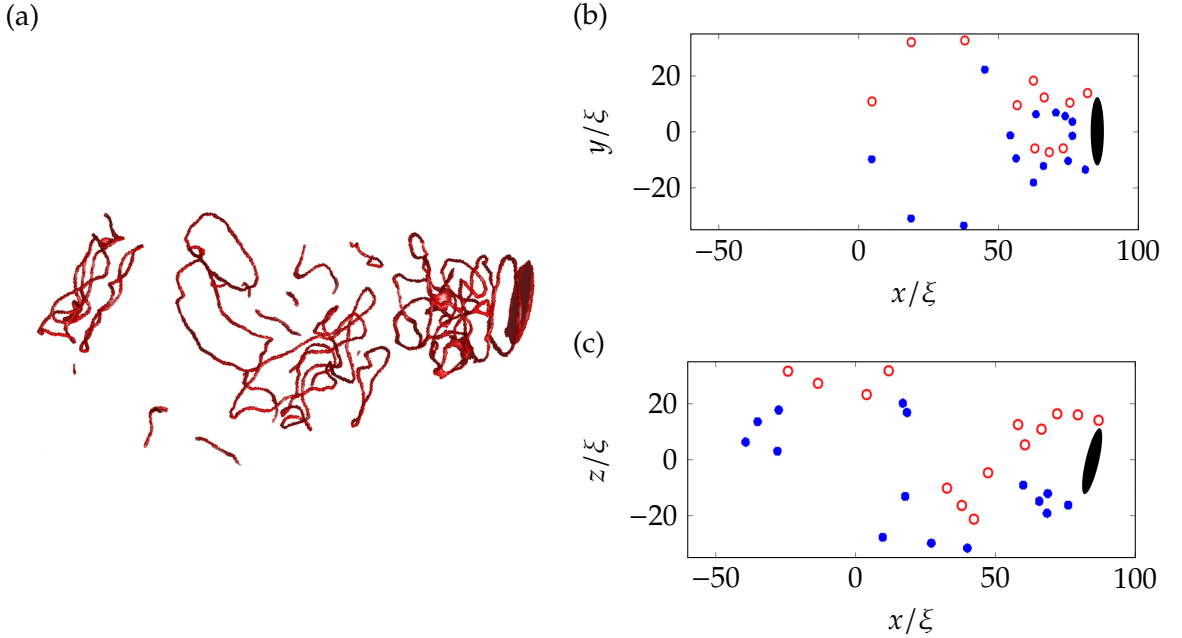


Figure 4.10: Asymmetric wake in 3D at $t = 340 (\xi/c)$ for an elliptical obstacle ($d = 5\xi$ and $\varepsilon = 5$) moving at $v = 0.6 c$. (a) Isosurface plot of low density, over a range $[-60, 100]$ in x and $[-25, 25]$ in y and z . (b) Vortex locations in the xy plane. (c) Vortex locations in the xz plane. In (b) and (c) red/blue denotes vortex lines with quanta of circulation $+1/-1$.

We break the cylindrical symmetry of the system by tilting the obstacle by a small angle in the xz plane. The vortex rings, illustrated in Figure 4.10, now eject and evolve asymmetrically; Kelvin waves and reconnections occur, forming an apparently disordered

tangle of vortices behind the obstacle. Due to the manner in which symmetry is broken, the wake remains approximately symmetric in the xy plane, as evident in Figure 4.10 (b). However, unlike in Figure 4.10, the vortices do not self organise into two clusters of alternate circulation. This is due to the vortex rings interacting, reconnecting and shifting out of the plane (which manifests in 2D as two alternate-sign vortices approaching one another).

However, in the xz plane (Figure 4.10 (c)), symmetry is broken. Due to the relatively high frequency of vortex nucleation and relatively low flow speed, like signed vortices cluster together as they are ejected by the obstacle, much like the 2D solutions seen in earlier sections. Downstream the tangle may shift both across or out of the plane. In 2D, although this manifests as a shift in location of the vortex clusters, the clusters largely remain rather than forming dipoles.

4.5 Conclusions

We have shown that the motion of an obstacle in a Bose-Einstein condensate produces classical-like wakes consisting of quantum vortices of the same polarity. This is consistently observed in both 2D and 3D scenarios. By modifying the obstacle so that it is elliptical, which reduces the critical velocity for vortex nucleation, vortices are generated at a sufficiently high rate that they undergo strong interactions with their neighbours (rather than being swept away). This leads to the production of classical-like wakes. Symmetric wakes resemble those observed in classical flow at low Re . These are unstable, forming time-dependent asymmetric structures similar to the Bénard–von Kármán vortex street of classical fluid dynamics. Vortex singularities in the inviscid superfluid thus mimic classical vortex patterns typical of viscous flows. The effects which we describe (dependence of the critical velocity and cluster size on the obstacle’s size, velocity and ellipticity) can be experimentally studied in atomic Bose-Einstein condensates using moving laser-induced potentials. They are also relevant to the motion of objects (such as vibrating wires, grids and forks) in superfluid helium, as the obstacle’s ellipticity plays a role which is analogous to rough boundaries [109, 110]. This idea is explored in detail in Chapter 7.

4.6 Further Work

4.6.1 A ‘quantum’ Reynolds number

The work in this chapter has been built upon and expanded by Reeves *et. al.* [53]. The group performed many 2D simulations using circular ($\varepsilon = 1$) Gaussian beams over a large parameter space of d and v . By applying the phase unwinding algorithm described in Section 3.5 to remove vortices from the periodic flow, the group performed many simulations

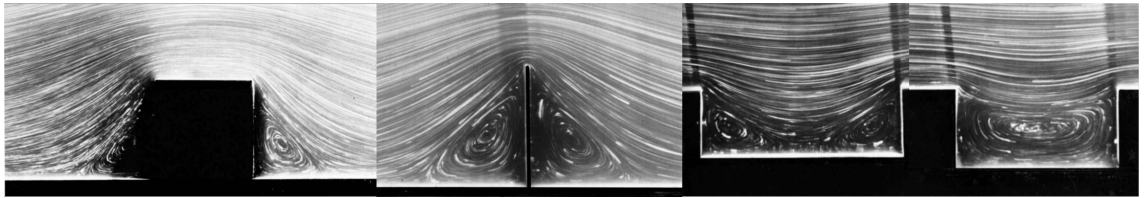


Figure 4.11: Various examples of classical viscous fluid flow around square obstacles and recesses [69].

at efficient resolutions with a high speed GPE numerical simulation GPU/CUDA code running on a cluster of graphics cards. The large number of simulations allowed Reeves *et. al.* to identify a ‘quantum’ Reynolds number, via dynamical similarity of a hard circular cylinder in classical viscous flow and superfluid flow in the presence of a soft Gaussian obstacle.

4.6.2 Other analogues

Many studies of classical viscous flow have been performed over the years. Collections such as Van Dyke’s *Album of Fluid Motion* [69] demonstrate the wide range of flows possible with various obstacle shapes and sizes in both 2D and 3D regimes. As an example, the wakes of rectangular (rather than circular) obstacles and recesses are shown in Figure 4.11. This chapter investigated the classical-like wakes in the simplest case of a cylinder in quantum flow. It would be an extremely interesting direction for future work to attempt to experiment with the more complicated examples of classical flow patterns that exist in the literature. The idea that the behaviour of many quantum vortices collectively reproduces classical physics would suggest that perhaps other analogies of classical fluid wakes exist in the quantum fluid realm.

Chapter 5

Decay of 2D quantum turbulence in a highly oblate Bose-Einstein condensate

5.1 Introduction

Ultracold gaseous Bose-Einstein condensates (BECs) provide a unique testbed with which to investigate the phenomenon of quantum turbulence and the more rudimentary realm of superfluid vortex dynamics [51, 111]. These systems provide an impressive degree of parameter manipulation unavailable in superfluid helium, the traditional context for studying quantum turbulence [112], with scope to control the particle interactions and potential landscape in both time and space. The typical size of these systems is only one or two orders of magnitude larger than the inter-vortex spacing, which in turn is another order of magnitude larger than the vortex core size. These compact length scales mean that the collective behaviour of vortices and their interaction with the background condensate is significant. The emergence of turbulent-like behaviour in the form of a vortex tangle was observed by Henn *et al.* in 2009 by oscillating a three-dimensional condensate [113]. What's more, the experimentalist's handle over the confining potential enables crossover to two-dimensional quantum turbulence [114]: by tightly confining the trap geometry along one axis, such that the vortices closely embody point vortices [115], states of two-dimensional quantum turbulence have been recently reported [116, 100].

In the recent experiment of Kwon *et al.* [100], a trapped, oblate BEC was translated past a stationary, laser-induced obstacle. As investigated in Chapter 4, vortices and anti-vortices were nucleated into the condensate once the relative speed exceeded a critical value [102], characteristic of superfluids. A state of two-dimensional quantum turbulence emerged, characterized by a disordered distribution of vortices. The authors monitored

the number of vortices, revealing the dependence on the relative speed and the thermal relaxation of the vortices. They directly observed vortex collision events, characterized by a crescent-shaped depletion in the condensate density. Furthermore, some vortex cores were seen to coalesce, evidence of vortex pair annihilation.

In this chapter we elucidate these experimental findings through mean-field simulations of the two-dimensional Gross-Pitaevskii equation (GPE), both at zero-temperature and in the presence of thermal dissipation, modelled through a phenomenological dissipation term. Notably, our simulations provide insight into the sign of the circulation of the vortices and the early-stage evolution, not accessible experimentally. We establish the key stages of the dynamics, from the initial nucleation of vortices and formation of a quasi-classical wake, through the rapid symmetry breaking and disorganization of the vortices, to the decay of the vortices by annihilation or passage out of the condensate.

5.2 Model

In the experiment, a ^{23}Na condensate with $N = 1.8 \times 10^6$ atoms was confined within a highly-oblate cylindrically symmetric harmonic trap $V_{\text{trap}}(x, y, z) = \frac{1}{2}m[\omega_r^2(x^2+y^2)+\omega_z^2z^2]$, with axial frequency $\omega_z = 2\pi \times 350$ Hz and radial frequency $\omega_r = 2\pi \times 15$ Hz (corresponding to an aspect ratio parameter $\omega_z/\omega_r \approx 23$) and where m denotes the atomic mass. A 2D mean-field description is strictly valid when the condition $Nal_z^3/l_r^3 \ll 1$ is satisfied, where $l_z = \sqrt{\hbar/m\omega_z}$ and $l_r = \sqrt{\hbar/m\omega_r}$ are the axial and radial harmonic oscillator lengths and a is the s -wave scattering length [117, 118]. For this experiment, $Nal_z^3/l_r^3 = 8.3$, i.e. the system remains 3D in nature. Nonetheless, the dynamics of the vortices is essentially 2D due to the suppression of Kelvin waves in the z -direction [119]. Therefore, we will adopt a 2D description throughout this chapter and show that it is sufficient to capture the experimental observations. It is worth noting that in the xy plane the condensate closely approximates a Thomas-Fermi (inverted parabola) density profile with radius $R_{\text{TF}} \approx 70\mu\text{m}$.

We parametrise the condensate by the 2D wavefunction $\psi(\mathbf{r}, t)$; the condensate density distribution follows as $n(\mathbf{r}, t) = |\psi(\mathbf{r}, t)|^2$. The wavefunction satisfies the GPE, Equation (2.1), as described in Section 2.2. For computational efficiency, the numerical simulations are performed using dimensionless quantities as described in Section 2.8.2. Quantities are made dimensionless by writing them in terms of the harmonic oscillator units: length in terms of the radial harmonic oscillator length l_r , energy in terms of $\hbar\omega_r$, and time in terms of inverse radial trapping frequency ω_r^{-1} . However, to remain relevant to the experimental work of Shin *et al.*, in this chapter we report all quantities in their full dimensional form.

We solve the GPE on a 1024×1024 grid, with grid spacing $0.27\mu\text{m}$ in both x and y , using the fourth-order Runge-Kutta method described in Section 3.1.1. We have verified that reducing the grid spacing has no effect on our results. The vortex core size is characterized

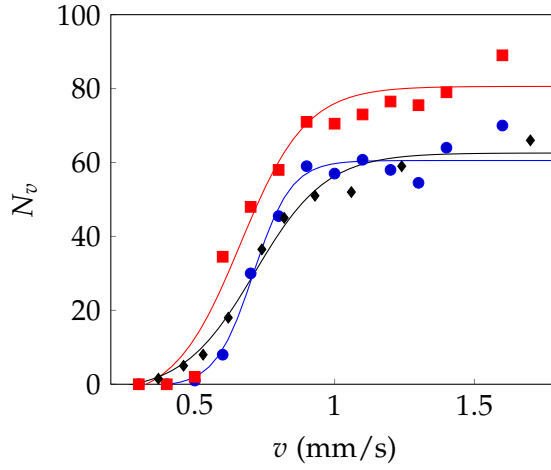


Figure 5.1: Number of vortices N_v in the condensate after removal of the obstacle. Shown are simulations of the GPE without dissipation (red squares), with dissipation $\gamma = 0.0003$ (blue circles) and experimental results extracted from Figure 1 of [100] (black diamonds). Sigmoid fits are also shown as dashed lines. Each point is averaged over 20 ms once the obstacle amplitude reaches $V_0 = 0$. For comparison, the speed of sound in the centre of the BEC is $v_c \approx 4.6$ mm/s.

by the healing length $\xi = \hbar/\sqrt{mn\bar{g}}$; at the condensate centre this has the value $\xi \approx 0.6\mu\text{m}$.

Following the experiment, the total potential acting on the condensate, $V(\mathbf{r}, t)$, is the above harmonic trap plus a static Gaussian-shaped circular obstacle potential of the form described in Section 2.15.2,

$$V_{\text{obs}}(\mathbf{r}) = V_0 \exp\left(-\frac{(x - x_0)^2}{d^2} - \frac{y^2}{d^2}\right), \quad (5.1)$$

with $V_0 = 15\mu\text{eV}$ and $d = 11.31\mu\text{m}$. The initial ground-state BEC is obtained by solving the GPE using the imaginary time method shown in Section 2.9, with an enforced norm of $N = 1.8 \times 10^6$ to match the experimental value. At $t = 0$ the harmonic trap is centred at $x_0 = 18.5\mu\text{m}$. The trap is translated towards the left, at speed v , over a distance of $37\mu\text{m}$; to smooth this speed curve we additionally include a linear acceleration/deceleration over 3.75ms at the start/end, which is included as part of the $37\mu\text{m}$ translation. Once the trap is at rest, the obstacle amplitude V_0 is ramped down to zero over 0.4s.

5.3 Number of Vortices Generated

Following removal of the obstacle, we determine the number of vortices in the system N_v using the methods described in Section 3.2. We limit our search to 75 percent of the Thomas-Fermi radius (centred on the centre-of-mass to account for sloshing motion); by avoiding the low density periphery we avoid artefacts from ghost vortices and match

closely what is performed experimentally (since vortices close to the edge are not detected due to low signal-to-noise [120]).

In Figure 5.1 we plot N_v versus the translation speed v . We see the same *qualitative* form between our simulations (red squares) and the experiment (black diamonds): above a critical speed $v_c \approx 0.45\text{mm/s}$ vortices enter the system, nucleated by the relative motion between the obstacle and the superfluid, and for $v > v_c$ the growth in N_v is initially rapid but tails off for $v \gg v_c$. Quantitatively, however, the GPE overestimates N_v . One can expect that thermal dissipation, not accounted for in the GPE, will act to reduce the number of vortices in the system. Experimental limitations in resolving and counting vortices may also contribute to the over-estimate of N_v from the GPE.

We include the effects of dissipation via the addition of phenomenological dissipation [21, 22], γ , which enters the GPE by replacing i on the left hand side by $(i - \gamma)$, a process formally derived in Section 2.11. This term induces the decay of excitations; for single vortices this manifests in them spiralling out of the trapped condensate [23, 119, 121, 122]. We choose a small value $\gamma = 0.0003$ so as to model the experiment in its very coldest realization of $T \sim 130\text{nK}$ and enforce the norm throughout the dissipative simulations so as to emulate the experiment (for which no significant loss of atom number was observed). With this dissipation the data for N_v becomes reduced (blue circles), bringing it closely in line with the experimental data.

5.4 Stages of the Condensate Evolution

We now examine in detail the evolution of the condensate, charting its dynamics from the initial stage (when the harmonic trap translation begins) to the intermediate and final stages (randomization and decay of the vortices). We see the same qualitative evolution with and without dissipation, and for all velocities exceeding v_c . For the purposes of illustration, we focus on an example with dissipation and a translation speed $v = 1.4\text{mm/s}$.

Figure 5.2 shows the condensate density at various times. At the start of the simulation ($t = 0$) the condensate has a smooth circular density profile, with a density depression due to the obstacle. Later vortices appear as small dots of low density; superimposed red/blue markers identify vortices of positive/negative circulation.

5.4.1 Vortex Nucleation and Wake Formation

To initiate the dynamics, the harmonic trap is translated to the left. This is performed sufficiently rapidly that the condensate does not adiabatically follow the trap minimum, but rather begins a sloshing motion in the trap; the centre-of-mass of the BEC oscillates at the trap frequency and the BEC undergoes a quadrupolar shape oscillation. As the BEC sloshes first to the left, its speed increases. When the local fluid velocity exceeds the

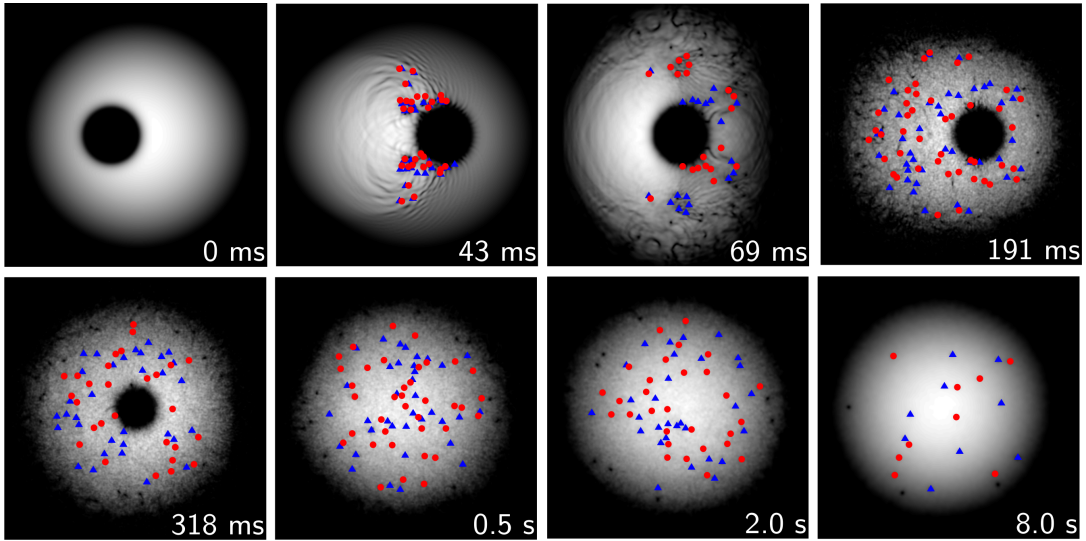


Figure 5.2: Snapshots of the condensate density, for a translational speed $v = 1.4\text{mm/s}$ and in the presence of dissipation ($\gamma = 0.0003$). The obstacle is completely removed at 0.43s. The field of view in each subfigure is of size $[170\mu\text{m}]^2$ and shifted along the x -axis so as to best display the condensate. Vortices with positive (negative) circulation are highlighted by red circles (blue triangles).

speed of sound, vortices nucleate [102] at the poles of the obstacle (where the local fluid velocity is the greatest) and are washed downstream (to the left). As seen in Chapter 4, the pattern of vortices nucleated by a moving obstacle in a superfluid depends, in general, on the speed, shape and size of the obstacle [84, 47, 123]. During the initial evolution vortices of negative and positive circulation are created near each pole in an irregular manner, sometimes with alternating circulation; other times several vortices of the same circulation appear. During this early stage ($t = 43\text{ms}$), vortices of opposite circulation may become very close and annihilate (i.e. undergo a 2D reconnection), leaving behind density (sound) waves. The condensate then sloshes to the right; this motion not only carries the existing vortices to the opposite (right) side of the obstacle but nucleates further vortices. As the condensate's sloshing mode is damped by the dissipation, the relative speed of the obstacle decreases and the vortex nucleation pattern changes: like-signed vortices are generated near each pole. In our case, the rate of vortex nucleation is sufficiently high that the like-sign vortices interact strongly with each other, collectively forming macroscopic clusters of negative and positive vortices near the object ($t = 69\text{ms}$). This is reminiscent of the wakes in classical viscous fluids past cylindrical obstacles [123]. As the condensate continues to slosh, more vortices nucleate into the system. It must be stressed that, up to these early times ($t = 191\text{ms}$), the vortex distribution remains symmetric about the x axis.

Without the dissipation term in the GPE, the sloshing mode initially decays while the obstacle is present but then persists with constant amplitude once the obstacle is removed.

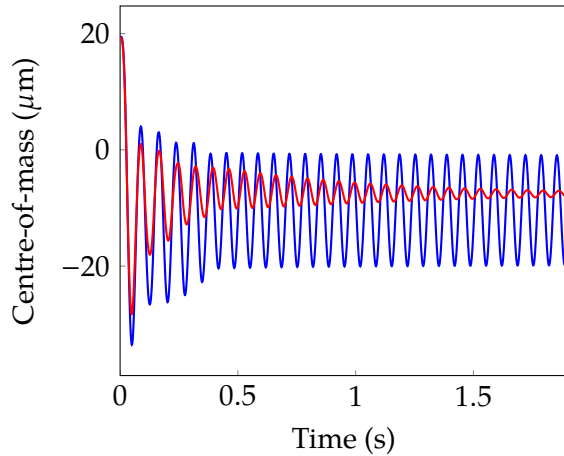


Figure 5.3: Centre-of-mass oscillations during condensate evolution for the BEC without the dissipation term (blue), and with a dissipation of $\gamma = 0.0003$ (red).

If dissipation is included then the sloshing mode continues to decay. Figure 5.3 shows the centre-of-mass oscillation over time, demonstrating the decay and that in either case, the sloshing mode is produced at the trap frequency.

5.4.2 Vortex Randomization

In the presence of the obstacle and the sloshing mode, vortices continually nucleate and their spatial distribution remains approximately symmetric about the x axis. At later times ($t > 318\text{ms}$) this symmetry breaks and the vortices evolve into a completely disorganized, apparently random configuration with no significant clustering of like-signed vortices. This random distribution of vortices is consistent with the experimental observations [100]; following this we also classify the system as one of quantum turbulence. Besides vortices, the condensate contains also collective modes and an energetic, disordered sound field, with this spatial range of excitations further indicative of two-dimensional quantum turbulence [114, 116]. (Note that the typical characteristic diagnostics of steady-state 2D quantum turbulence, e.g. power-law energy spectra and the inverse energy cascade, are not appropriate here since the system is not continuously driven and does not reach steady state.)

The vortex randomization is driven by the growth of numerical noise. We have repeated our results in the presence of imposed noise (amplitude 5%, as described elsewhere [123]) and find the qualitative dynamics to be unchanged (although, as one would expect, the vortex randomization occurs at a slightly earlier time). This noise serves to model the natural fluctuations that arises in a realistic experimental scenario, e.g. due to thermal and quantum atomic fluctuations, electromagnetic noise, vibrations, etc.

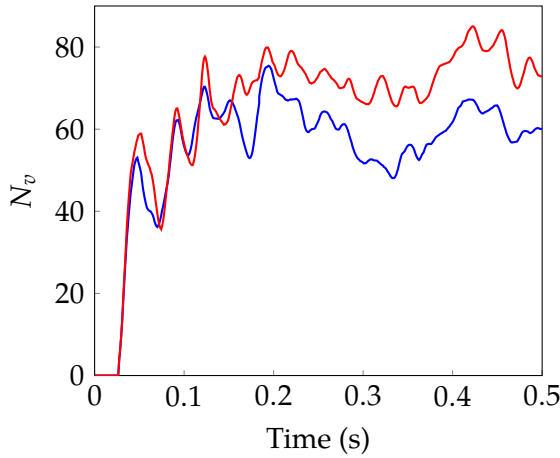


Figure 5.4: Growth of vortex number (in a single realization) at early times for a translational speed of $v = 1.4\text{mm/s}$. Shown are the results with no dissipation (blue) and with dissipation $\gamma = 0.0003$ (red).

It is interesting to note the obstacle is still in the system at this point, nucleating vortices in a symmetrical manner. The disorganised vortices already in the system create a velocity field which quickly mixes newly created vortices nucleated at the poles of the obstacle. Visual inspection, confirmed by the RCA clustering-detection algorithm [48, 49] described in Section 3.3.3, shows no significant clusters beyond this stage of the evolution. By the time the obstacle is removed the vortex configuration is essentially random, but the number of positive and negative vortices stays approximately equal. It is important to remark that, without detecting the sign of the vortex circulation, we could not reach these conclusions.

5.4.3 Vortex Decay

It is clear from Figure 5.2 that, following the removal of the obstacle, the number of vortices, N_v , depletes. Indeed, one expects that the condensate will decay towards its vortex-free, time-independent ground state. To quantify the vortex generation and decay, Figure 5.4 plots the growth of N_v at early times, and Figure 5.5 (a, b) plots the decay of vortices over the remaining experimental time period. The onset of vortex nucleation is at around $t = 0.02\text{ms}$; this is the time taken for accelerating condensate to exceed the speed of sound at the poles of the object. At first N_v grows steeply, as vortices (around 40-60) are rapidly driven into the system. Subsequently, N_v grows more slowly; vortices continue to be nucleated from the obstacle but vortices undergo annihilation or move into low density regions where they are not detected. The fluctuations in N_v are amplified, particularly at early times, by the shape oscillations of the condensate, which carry vortices in and out of the detection radius. As the obstacle is removed, the surrounding condensate fills the low density area. Vortices (including some outside of the detection radius) move inwards

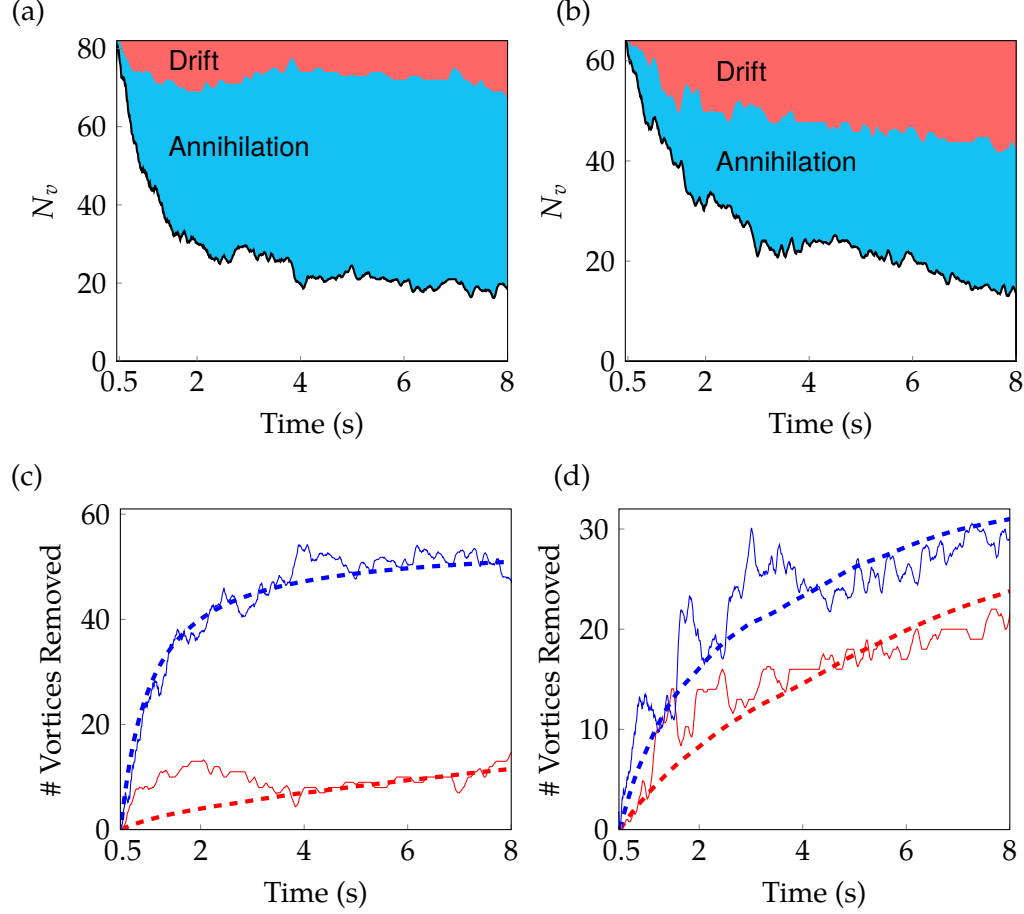


Figure 5.5: Vortex decay in the absence of dissipation (a, c) and with dissipation $\gamma = 0.0003$ (b, d) for a translational speed of $v = 1.4\text{mm/s}$. The upper figures show the decay of the total vortex number $N_v(t)$, with the contribution of drifting and annihilation depicted by the shaded regions. The lower figures show the drift number $N_d(t)$ and annihilation number $N_a(t)$, plus their respective fits.

with the condensate, causing N_v to peak at $t \approx 0.4\text{s}$. Following removal of the obstacle, the vortex number N_v decays with time. This is shown in Figure 5.5(a) and (b) for the absence and presence of dissipation, respectively.

Kwon's decay model

Kwon *et al.* [100] argued that there are two mechanisms by which vortices decay: (i) thermal dissipation (resulting in drifting of vortices to the edge of the condensate), and (ii) vortex-antivortex annihilation events, and proposed that the vortex decay takes the form:

$$\frac{dN_v}{dt} = -\Gamma_1 N_v - \Gamma_2 N_v^2. \quad (5.2)$$

Here the linear and nonlinear terms, parametrised by the positive coefficients Γ_1 and Γ_2 , respectively, model these two decay processes. From our simulations we are able to independently count the number of vortices which drift out and the number which annihilate. We decompose the number of vortices according to

$$N_v(t) = N_i - N_d(t) - N_a(t), \quad (5.3)$$

where N_i is the initial number of vortices (when the obstacle is removed), $N_d(t)$ is the cumulative number of vortices which have drifted out of the condensate and $N_a(t)$ is the cumulative number which have undergone pair annihilation. The contribution of both vortex drifting and annihilation to the overall decay of N_v is depicted by the coloured regions in Figure 5.5(a) and (b). In the absence of dissipation the vortex decay is dominated by annihilation. Indeed, apart from at early times (where internal condensate dynamics carry vortices out to high radii), no vortices drift out. In contrast, in the presence of dissipation, vortices continue to drift out over time, consistent with dissipative dynamics of single vortices [121].

Unfortunately, fitting $N_v(t)$ directly to Equation (5.2) leads to inconclusive results. While we find that the best-fitting solutions fit the data well, the resulting values for Γ_1 are found to be negative, corresponding to a positive growth. Considering that Γ_1 is a term associated to thermal dissipation there is no reason to expect a growth here. We interpret this inconsistency as resulting from fitting Equation (5.2) directly; the meaning of the rates Γ_1 and Γ_2 (i.e as characterising rates of vortex loss through drifting and vortex-antivortex annihilation) are not enforced, and so the best-fit parameters cannot be used to infer anything about the physical processes.

Our solution is to enforce the meaning of Γ_1 and Γ_2 while performing the fitting process. The decomposition of N_v as Equation (5.3) enables us to independently fit the drift and annihilation decay processes as two coupled ODEs for N_d and N_a ,

$$\frac{dN_d}{dt} = \Gamma_1 N_v, \quad \frac{dN_a}{dt} = \Gamma_2 N_v^2. \quad (5.4)$$

By taking the time derivative of Equation (5.3) and substituting in Equation (5.4), Equation (5.2) can be recovered. As a consequence of fitting the coupled ODEs independently, the physical meaning of each rate term is enforced. To further fix the physical meaning, the fitted value of both Γ_1 and Γ_2 are forced to be positive (corresponding to a vortex decay over time). The vortex decomposition along with the each independent fit is shown in Figure 5.5(c) and (d) for the absence and presence of dissipation, respectively. We find that the rate equation fits fairly well most cases, although finds difficulty in fitting the lack of vortex decay via drifting when $\gamma = 0$.

In the absence of dissipation we find a value of $\Gamma_1 = 5.5 \times 10^{-2}$. However, it is not

appropriate to discuss the physical meaning of Γ_1 in this case, since $\gamma = 0$ and so N_d is not of a decaying form; this also explains the less successful fit for N_d in the absence of dissipation. We also find the corresponding $\Gamma_2 = 9.7 \times 10^{-3}$. While the experimental observations [100] suggest Γ_2 is proportional to T^2 and thus approaches 0 as $T \rightarrow 0$, our results demonstrate a finite Γ_2 in this limit.

With the inclusion of a dissipation of $\gamma = 0.0003$ we obtain $\Gamma_1 = 12.3 \times 10^{-2}$, this corresponds to an increase to the rate of vortex decay via the drifting out mechanism, as expected when introducing dissipation into the system [121]. We also find $\Gamma_2 = 5.3 \times 10^{-3}$. These values are in good agreement with the values obtained by Kwon *et al.* when fitting to their coldest experiments.

Modified decay model

We have shown that the rate equation proposed by Kwon *et al.* [100], Equation (5.2), can be used to characterise the decay of vortices via two mechanisms: a rate of decay due to drifting, and a rate of decay due to annihilation. However, to obtain physically realistic fits, we were forced to enforce the meaning of the two decay terms as part of the fitting mechanism, a process which is not ideal.

Post publication [124] of the results in this chapter, several authors [125, 126] independently investigated vortex interactions in the context of quantum turbulence, providing arguments and evidence to support modified rate equations for the decay of vortex number in atomic BEC experiments. Recently, Cidrim *et al.* [125] proposed a scheme for generating two-dimensional quantum turbulence with the novelty of controlling the *polarisation* of the resulting turbulence by the addition of small localised repulsive potentials. Similarly to our findings in Section 5.4.3, fitting to Equation (5.2) without enforcing the meaning of the terms provided physically unrealistic decay rates. Cidrim *et al.* proposed a simple argument that takes into account the polarised nature of the turbulence and early-time steeper-than-quadratic effects, providing the following phenomenological model of vortex decay,

$$\begin{aligned} \frac{dN_+}{dt} &= -\Gamma_3 N_+^{3/2} - \Gamma_4 (N_+ N_-)^2, \\ \frac{dN_-}{dt} &= -\Gamma_3 N_-^{3/2} - \Gamma_4 (N_+ N_-)^2, \end{aligned} \quad (5.5)$$

where N_+/N_- are the number of vortices of positive/negative circulation, so that $N_v = N_+ + N_-$. Fitting to this model gave physically realistic values for both decay rates in all of their simulated cases. For the unpolarised turbulence that we investigate, Equation (5.5)

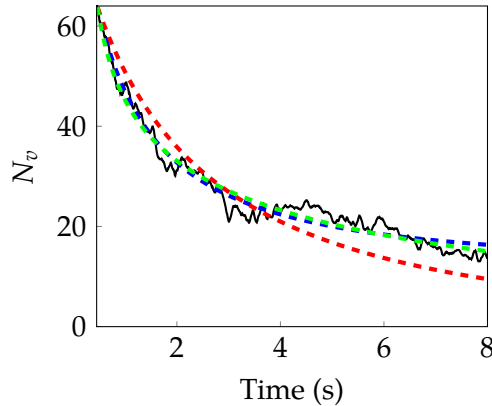


Figure 5.6: Comparison of the three vortex decay models introduced in this chapter. Shown is the decay of vortex number for our GPE simulation with dissipation $\gamma = 0.0003$ and a translational speed of $v = 1.4\text{mm/s}$. (black solid line). Also shown is fits to the data using Kwon's rate equation (blue dashed line), Kwon's rate equation while enforcing the meaning of the decay rates (red dashed line) and Cidrim's equation (green dashed line).

can be equivalently written as

$$\frac{dN_v}{dt} = -\Gamma_3 N_v^{3/2} - \frac{\Gamma_4}{8} N_v^4. \quad (5.6)$$

Groszek *et al.* independently provided evidence [126] that vortex annihilation events are in fact a four-body loss mechanism, leading to an annihilation decay rate of the form $dN_v/dt \sim -N_v^4$, supporting the findings of Cidrim *et al.*

As a further test of Cidrim's modified decay law we have fitted Γ_3 and Γ_4 to our simulation with dissipation $\gamma = 0.0003$ and trap speed $v = 1.4\text{mm/s}$. A comparison of the resulting decay rates is shown in Table 5.1, and the fits are visually compared in Figure 5.6. Kwon's equation [Equation (5.2)] provides a good qualitative fit to the decay rate overall, but physical processes cannot be inferred from the resulting values of the decay rates Γ_1 and Γ_2 . Enforcing the meaning of the terms in Kwon's equation by fitting $N_d(t)$ and $N_a(t)$ independently [Equation (5.4)] performs the least favourably overall, but provides physically realistic decay rates. Finally, Cidrim's equation [Equation (5.6)] qualitatively fits *at least* as well as Kwon's equation, while having the advantage of physically realistic values for the decay rates and the ability to handle non-zero turbulence polarity. We note that our resulting values for Γ_3 and Γ_4 when fitted to Cidrim's equation compare well to values obtained by Cidrim *et al.* when fitting to decaying 2D turbulence with zero polarisation and $N_v(0) \sim 150$. These results suggest that of the fitting methods described, Cidrim's Equation is the best performing phenomenological model of vortex decay.

<i>Decay rate</i>	<i>Kwon's equation</i>	<i>Decomposed Kwon's equation</i>	<i>Cidrim's equation</i>
Drift	$\Gamma_1 = -1.8 \times 10^{-1}$	$\Gamma_1 = 12.3 \times 10^{-2}$	$\Gamma_3 = 2.0 \times 10^{-2}$
Annihilation	$\Gamma_2 = 1.4 \times 10^{-2}$	$\Gamma_2 = 5.3 \times 10^{-3}$	$\Gamma_4 = 3.3 \times 10^{-6}$

Table 5.1: Comparison of the resulting decay rates when fitting Kwon's equation [Equation (5.2)], decomposed Kwon's equation [Equation (5.4)] and Cidrim's equation [Equation (5.6)] to the decay of vortex number for our GPE simulation with dissipation $\gamma = 0.0003$ and a translational speed of $v = 1.4\text{mm/s}$.

5.5 Crescent-Shaped Density Structures

In the experiment, Kwon *et al.* observed the occasional appearance of crescent-shaped waves of depleted density. Lacking direct access to the vortex signs, they suggested that these structures result from annihilation events of vortices of opposite circulation [127–129]: a vortex reconnection is predicted to induce an intense, localised, rarefaction sound pulse [130, 131]. Figure 5.7 shows snapshots of the condensate density and phase during a reconnection event. Vortices show up as localized dips in the density (upper row) and 2π -defects in the phase (lower row). Figure 5.7 (a) shows a vortex (A) and antivortex (B) close to each other, and a third vortex (C) in the vicinity. Note that the individual vortices are not spatially resolvable through their density alone (the vortex cores merge into a deep, elongated crescent-shaped depression), but they are clearly identified by the phase plot. A short time later (b), vortices A and B annihilate, as confirmed by the disappearance of their phase singularities, leaving behind a shallow rarefaction pulse (S) with a linear phase step. This pulse rapidly evolves into a shallow, crescent-shaped sound wave [Figure 5.7 (c)]. In other words, our simulations yield crescent-shaped density features as seen in the experiment, but these features are not uniquely formed by annihilation events – they may also result from two (or more) vortices in close proximity. Information about the condensate phase is thus crucial to distinguish the nature of these observed structures. In this direction, an approach has recently been proposed for the experimental detection of quantized vortices and their circulation in a 2D BEC [132].

5.6 Vortex Generation via an Elliptical Obstacle

It is evident from the snapshots in Figure 2 that the initial translation of the condensate past the obstacle generates not just vortices but also shape excitations, sound waves (low-amplitude density waves), and high-amplitude density waves. These additional excitations will heat the condensate and modify the subsequent turbulent dynamics in a highly nonlinear and complicated manner. While reducing the translational speed reduces this disruption, this also reduces the number of vortices. A less disruptive and more efficient (higher rate of vortex nucleation) means to generate vortices may be provided by employ-

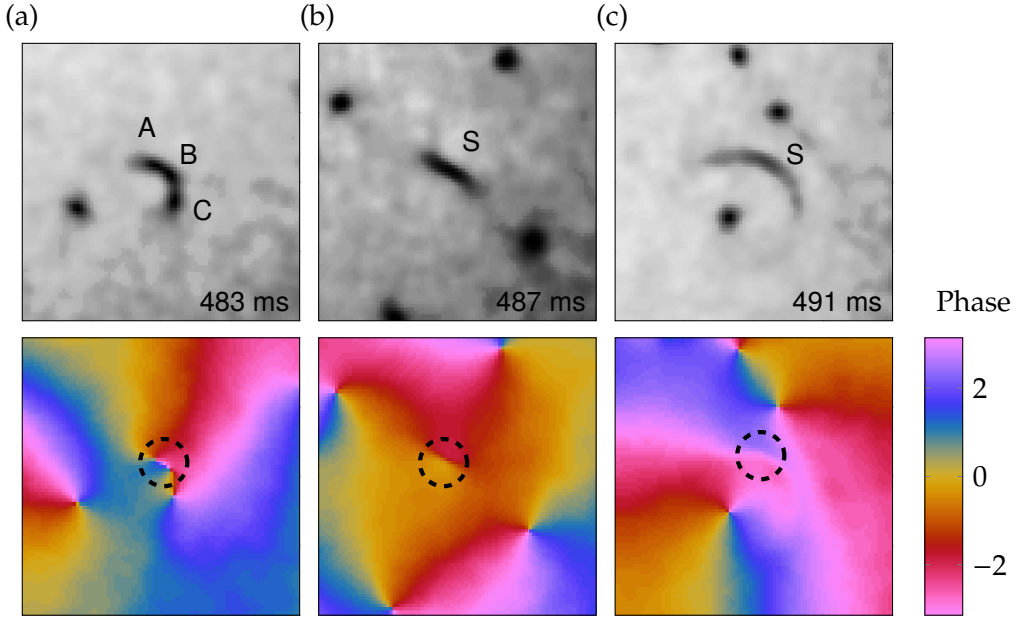


Figure 5.7: Density (upper) and phase (lower) just before (a), immediately following (b) and a later time after (c) a vortex-antivortex annihilation event. The field of view is $[23.5\mu\text{m}]^2$, surrounding the vortex pair/sound pulse (highlighted by a circle in the phase).

ing a laser-induced obstacle of a form similar to that used in Chapter 4, with an *elliptical* rather than circular cross-section (experimentally attainable through cylindrical beam focusing).

Repeating our simulations with such an elliptical obstacle, governed by Equation (2.45), with arbitrary ellipticity $\epsilon = 3$ (the short/long axis being parallel/perpendicular to the flow) confirms the same qualitative behaviour as in Chapter 4 for homogeneous systems [123]: the ellipticity acts to reduce the critical superfluid velocity and, for a given flow speed, increase the rate of vortex nucleation. To illustrate the merits of the elliptical obstacle, in Figure 5.8 we depict snapshots of the condensate dynamics for ellipticity $\epsilon = 3$ and a translational speed of $v = 0.8\text{mm/s}$. Despite a lower translational speed, the number of vortices generated by the time the obstacle is removed is almost identical to the circular example of Figure 5.4. As a consequence of the reduced translational speed, the condensate disruption is visibly reduced. It is also worth noting that the elliptical obstacle promotes the formation of clusters of like-signed vortices (see intermediate time), and thus may facilitate future exploration of coherent vortex structures.

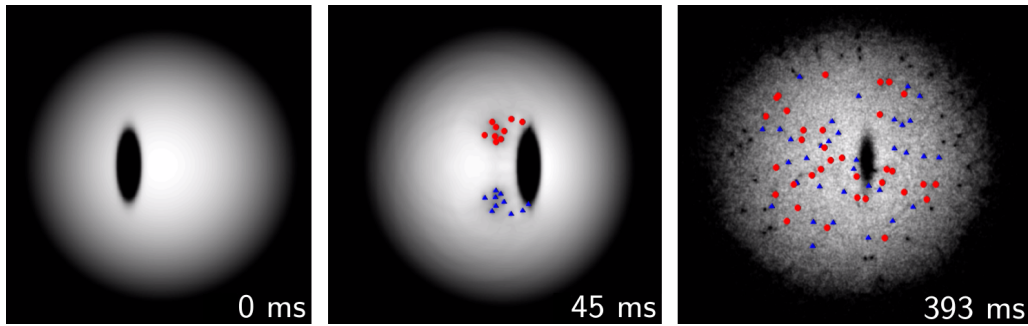


Figure 5.8: Snapshots of the condensate density for a translational of speed $v = 0.8\text{mm/s}$ past an elliptical obstacle (ellipticity $\epsilon = 3$). The field of view in each subfigure is of size $[170\mu\text{m}]^2$ and shifted along the x -axis so as to best display the condensate. Compared to the corresponding snapshots in Figure 5.2, the elliptical obstacle generates as many final vortices but at a lower translational speed and with reduced condensate disruption.

5.7 Conclusions

In conclusion, we have shown that the recent experimental creation and decay of vortices within a BEC [100] is well described by simulations of the 2D GPE with phenomenological dissipation (despite the 3D nature of the system). Theoretical access to the condensate phase, and thus the circulation of the vortices, promotes our understanding of the dynamics. In the early stages of translation of the obstacle, a quasi-classical wake of vortices forms behind it, before symmetry breaking causes disorganisation of the vortices. After the obstacle is removed, the vortices decay in a manner which is consistent with the two mechanisms proposed by Kwon *et al.*, i.e. loss of vortices at the condensate edge due to thermal dissipation and vortex-antivortex annihilation events within the condensate.

We fit the vortex decay the rate equations proposed by Kwon *et al.* and Cidrim *et al.* In the case of Kwon's equation we enforce the meaning of the decay rates to find values comparable to the coldest experiments of Kwon *et al.* In the case of fitting to Cidrim's modified equation, we find rates comparable to the simulations of Cidrim *et al.* without the need to enforce meaning. We conclude that Cidrim's equation fits to the data most favourably, while providing physically realistic values for the decay rates.

We confirm the occasional appearance of crescent-shaped density features, resulting either from the proximity of vortex cores or from a sound pulse which follows a vortex-antivortex reconnection. Finally, we propose that a moving *elliptical* obstacle may provide a cleaner and more efficient means to generate two-dimensional quantum turbulence.